



Exceptional sea ice loss leading to anomalously deep winter convection north of Svalbard in 2018

Chuanshuai Fu¹ · Paul G. Myers¹

Received: 10 February 2023 / Accepted: 15 November 2023 / Published online: 21 December 2023
© The Author(s) 2023

Abstract

An important question is will deep convection sites, where deep waters are ventilated and air-gas exchange into the deep ocean occurs, emerge in the Arctic Ocean with the warming climate. As sea ice retreats northward and as Arctic sea ice becomes younger and thinner, air-sea interactions are strengthening in the high-latitude oceans. This includes new and extreme deep convection events. We investigate the associated physical processes and examine impacts and implications. Focusing on a region near the Arctic gateway of Fram Strait, our study confirms a significant sea ice cover reduction north of Svalbard in 2018 compared to the past decade, shown in observations and several numerical studies. We conduct our study using the regional configuration Arctic and North Hemisphere Atlantic of the ocean/sea ice model NEMO, running at 1/12° resolution (ANHA12). Our numerical study shows that the open water condition during the winter of 2018 allows intense winter convection over the Yermak Plateau, as more oceanic heat is lost to the atmosphere without the insulating sea ice cover, causing the mixed layer depth to reach over 600 m. Anomalous wind prior to the deep convection event forces offshore sea ice movement and contributes to the reduced sea ice cover. The sea ice loss is also attributed to the excess heat brought by the Atlantic Water, which reaches its maximum in the preceding winter in Fram Strait. The deep convection event coincides with enhanced mesoscale eddy activity on the boundary of the Yermak Plateau, especially to the east. The resulting substantial heat loss to the atmosphere also leads to a heat content reduction integrated over the Yermak Plateau region. This event can be linked to the minimum southward sea ice volume flux through Fram Strait in 2018, which is a potential negative freshwater anomaly in the subpolar Atlantic.

Keywords Deep convection · Meridional overturning circulation · Arctic Ocean · Ocean modelling · Sea ice loss · Air-sea interaction

1 Introduction

The Atlantic Water (AW) is a warm and saline water mass that originates from the North Atlantic Ocean. While cold and fresh Arctic Water and Arctic sea ice are exported out of the Arctic Ocean by the East Greenland Current on the west side of Fram Strait (Karpouzoglou et al. 2022; Sumata et al. 2022), AW is the main source of heat and salt to the Arctic Ocean. It is carried by the West Spitsbergen Current (WSC) on the east side of Fram Strait west of Svalbard (Beszczynska-Möller et al. 2012). The mean volume and heat transport through Fram Strait were estimated from mooring arrays

to be 3.0 ± 0.2 Sv over 1997–2010 (Beszczynska-Möller et al. 2012) and 26–50 TW over 1997–2006 (Schauer et al. 2008), respectively. The AW in the WSC has exhibited a warming trend for the period of 1997–2010 (Beszczynska-Möller et al. 2012), and the increased heat transport has the potential to warm the intermediate AW layer in the Arctic Ocean (Polyakov et al. 2012) and melt more Arctic sea ice (Polyakov et al. 2010), in particular the sea ice near the Arctic gateway of Fram Strait.

The AW circulation is an integral part of the process regulating the oceanic dynamics near Fram Strait and over the Yermak Plateau where the regional bathymetry is complex (Fig. 1). Not all of the AW arriving at Fram Strait flows into the Arctic Ocean proper. Recirculations in Fram Strait reduce the amount of heat brought into the Arctic Ocean. The northern AW recirculation branch has a strong seasonal variability, which appears to be directly ascribed to the

✉ Chuanshuai Fu
chuanshu@ualberta.ca

¹ Department of Earth and Atmospheric Sciences, University of Alberta, Edmonton, AB, Canada

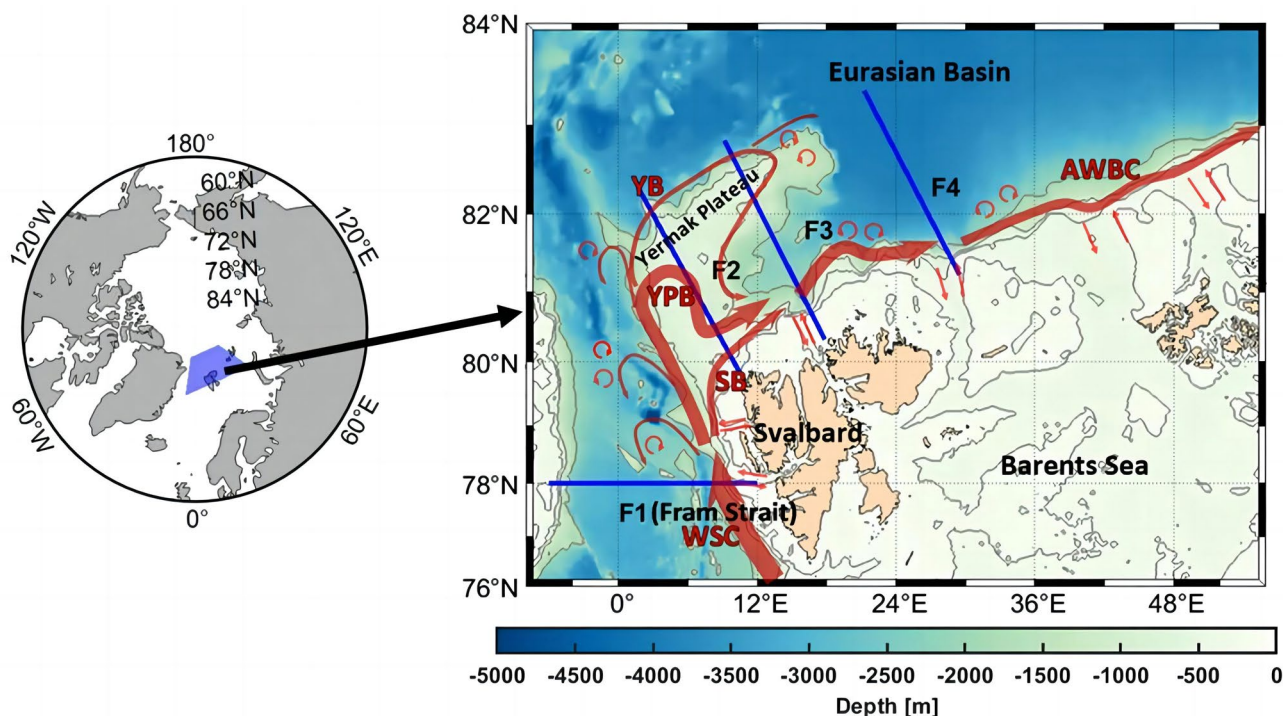


Fig. 1 The schematic circulation of the AW over the Yermak Plateau and in the Western Eurasian Basin with major geographic features labelled. Four sections (F1, F2, F3, F4) are shown in blue lines. Section F1 represents the Arctic gateway of Fram Strait. Grey contour lines are -200 m, -500 m, -1000 m and then -2000 m. Red

arrows along the slope in the opposite direction represent shelf-slope exchanges. Red circling arrows indicate AW eddy activity. WSC: West Spitsbergen Current; SB: Svalbard Branch; YPB: Yermak Pass Branch; YB: Yermak Branch; AWBC: AW Boundary Current. The map is adapted from Athanase et al. (2020)

seasonally varying eddy activity that also promotes the AW subduction beneath the ice edge (Hattermann et al. 2016; Wekerle et al. 2017). The seasonal increase in eddy activity is manifested by the strong Eddy Kinetic Energy (EKE) during winter months (Von Appen et al. 2016).

In addition to the AW recirculation branches, the AW entering the Arctic Ocean splits into three primary pathways north of Svalbard (Fig. 1), including the Yermak Pass Branch, the deep Yermak Branch, and the shallow Svalbard Branch (Cokelet et al. 2008; Crews et al. 2019; Gascard et al. 1995; Koenig et al. 2017a, b; Menze et al. 2019; Pérez-Hernández et al. 2019). A warmer and thereby less dense AW in Fram Strait forms a strong potential vorticity barrier that promotes more inflow of the Yermak Pass Branch and less AW recirculation (Von Appen et al. 2016; Chatterjee et al. 2018; Crews et al. 2019). Crews et al. (2019) found that the warming trend of ~ 0.5 °C/decade in the AW through Fram Strait can potentially change the division between the Yermak Pass Branch (as the dominant AW branch among three AW branches) and the recirculation portion, thus bringing more heat into the Arctic Ocean at a faster rate.

The AW is cooled and freshened through a number of other processes such as atmospheric surface cooling, sea ice melt, convective mixing, lateral eddy fluxes and exchanges

with shelf water and trough outflows (Athanase et al. 2020; Boyd and D'Asaro 1994; Koenig et al. 2018; Onarheim et al. 2014). By studying mechanisms that contribute to the cooling of the WSC off west of Svalbard, Boyd and D'Asaro (1994) presented that the AW near the surface is transformed into colder or fresher water masses by atmospheric surface cooling and by sea ice melting. The production of the fresher water mass strengthens the stratification and then partially insulates the warm core from surface cooling. Even so, the cooling in the interior of the WSC is enhanced by the eddy-driven mixing. Exchanges with shelf water and trough outflows can modulate the hydrographic changes in the AW along slopes and on shelves. Nilsen et al. (2016) showed half of the AW heat loss is owing to heat loss to the ambient colder water masses. The changes in the AW properties of the WSC fundamentally affect the heat input to the Arctic Ocean proper.

The region north of Svalbard, downstream of Fram Strait, is where the warm AW inflows can further directly interact with the sea ice (Ivanov et al. 2012, 2018; Onarheim et al. 2014; Rudels et al. 2015). As a result, the AW is severely transformed and modified into a less warm and saline water mass in the upper layer. Onarheim et al. (2014) found that the sea ice concentration has shown a conspicuous decline north

of Svalbard during winter since 1979. This corresponds with the trend of the increasing AW temperature and winter air temperature. The local wind does not contribute to the trend but has an impact on the interannual variability of the sea ice concentration (Onarheim et al. 2014). Ivanov et al. (2012) indicated that the shrinking ice cover can also be linked to the monotonic increase in the AW temperature in Fram Strait. The winter heat loss to the atmosphere is principally supplied by the upward heat flux from the AW layer through convective mixing, so vertical convection plays a significant role in shaping the thermohaline structure and melting winter sea ice (Ivanov et al. 2012, 2018). This has been examined by Koenig et al. (2017a, b) who demonstrated the modelled convection-induced upward heat fluxes contribute to the interannual variability of winter sea ice edge location. While a general relationship among the above-mentioned processes has been proposed in this region, a detailed analysis of the extreme events concerning the oceanic condition change and their mechanisms and potential impacts have not been completely explored in previous studies.

The three AW inflows merge into the AW boundary current north of Svalbard and flow along the rim of the Eurasian Basin (Athanasé et al. 2021). Pérez-Hernández et al. (2019) investigated the characteristic seasonality of the AW boundary current over 2012–2013 at the A-TWAIN array at 30° E. The strong seasonality can be explained by the fact that the AW is modified and transformed locally due to the convective mixing during winter and early spring (Pérez-Hernández et al. 2019). Similar to the upstream WSC, the AW boundary current is baroclinically unstable, which is indicated by the meandering of the current (Pérez-Hernández et al. 2017; Våge et al. 2016). Numerous eddies (mostly anticyclones) that were spawned by the current have been observed from shipboard sections (Pérez-Hernández et al. 2017; Våge et al. 2016) and simulated by the model-based studies (Athanasé et al. 2019; Crews et al. 2018). Eddies shed from the AW boundary current erode the AW thermohaline signature.

Focusing on the Yermak Plateau north of Svalbard (Fig. 1), we explore the exceptional sea ice reduction in 2018 compared with other years between 2008 and 2019. It is commonly known that no sea ice cover appears west of Svalbard due to the great amount of heat brought by the WSC, whereas it is often covered by sea ice in the north of Svalbard. This study is motivated by more frequent and longer-lasting events of sea ice retreat north of Svalbard in recent years, and the thinner and younger ice has been examined to respond more and more strongly and tightly to the local winds on top as well as the AW heat below (Ivanov et al. 2016; Koenig et al. 2017a, b; Lundesgaard et al. 2022; Athanasé et al. 2020). Using a 1/12° ocean model simulation (Mercator Physical System), Athanasé et al. (2020) presented extremely low sea ice concentration over the Yermak Plateau, causing the averaged Mixed Layer Depth

(MLD) to be over 300 m depth in the winter of 2018. Here we use an eddy-permitting ocean/sea ice model simulation of 1/12° resolution (ANHA12) forced with different atmospheric forcing fields but also without sea ice assimilation, to reproduce the unprecedented sea ice cover reduction north of Svalbard in 2018. The reproducibility of the event in a free-running forced ocean model ascertains that such an extreme event is a robust feature. We bridge the knowledge gap in previous studies by investigating the physical processes affecting the anomalously deep convection north of Svalbard in 2018 and further examining the impacts and implications of the event. The event is an indication of deep winter convection and thus greater MLD and intermediate/deep water formation expanding northward into the Arctic Ocean.

The paper is organized as follows: Sect. 2 provides a brief description of the model simulation and presents the methods that we use for the calculations. Section 3 introduces the observational datasets. Section 4 serves as a model evaluation. In Sect. 5, we confirm the exceptional sea ice reduction that caused the deep convection north of Svalbard in the winter of 2018, and explain its causes by the mechanical process from winds and the thermodynamic process with the heat brought by the AW. We then demonstrate the AW properties change during the deep convection from three model sections north of Svalbard. This coincides with extremely high mesoscale eddy activity on the eastern boundary of the Yermak Plateau. We also suggest a potential link to the minimum southward sea ice flux through Fram Strait in 2018. Lastly, Sect. 6 concludes the study and discusses its implications for the northward migration of the Atlantic Meridional Overturning Circulation (AMOC).

2 Numerical methods

2.1 Model setup

We utilize the output data from the coupled ocean-sea ice model Nucleus for European Modelling of the Ocean (NEMO; available at <https://www.nemo-ocean.eu>) for numerical analysis. Two major embedded engines of the NEMO are Ocean Parallel Elastic (OPA) and Louvain-la-neuve Ice Model version 2 (LIM2). The former is the three-dimensional, C-grid and primitive-equation ocean general circulation model, whilst the latter is the three-layer (two layers of ice and one layer of snow) sea ice model with a modified elastic-viscous plastic ice rheology, both including the representations of the thermodynamic and dynamic processes (Fichefet and Maqueda 1997; Hunke and Dukowicz 1997; Madec 2016). A subdomain configuration of NEMO, named the Arctic and Northern Hemisphere Atlantic (ANHA), is primarily employed to carry out the numerical simulations.

The model mesh is extracted from the global ORCA tripolar grid, covering the whole Arctic Ocean, the North Atlantic Ocean and part of the South Atlantic Ocean with two open boundaries: one in the Bering Sea and the other at 20° S. There are 1632 * 2400 grid points at each horizontal level with an eddy-permitting resolution of 1/12° (hereafter ANHA 12), which gives a resolution of ~4.5 km in the Nordic Seas and ~4.2 km north of Svalbard. ANHA12 has 50 levels with layer thickness increasing from 1.05 m for the first level to 453.14 m at the bottom in a gradient manner. The integration period of the ANHA12 simulation used in this paper starts from January 2002 to the end of December 2021 with 5-day average output. The high temporal (hourly) and spatial (33 km) resolution atmospheric forcing acting on the sea surface, including 10-m surface wind, 2-m air temperature, and specific humidity, total precipitation as well as surface downwelling shortwave and longwave radiative fluxes, are taken from the Canadian Meteorological Centre's (CMC) Global Deterministic Prediction System (GDPS) ReForcasts (CGRF) dataset (Smith et al. 2014). These forcing fields are linearly remapped onto the model grid, significantly improving the model fidelity, and adding credibility to the analysis. Further information regarding the initial conditions and open boundary conditions can be found in Fu et al. (2023). The computation of the Mixed Layer Depth (MLD) in ANHA12 is based on a density difference of 0.01 kg/m³ with the surface (Da Costa et al. 2005; Thomas et al. 2015).

2.2 Sea ice and freshwater transport calculation

Monthly sea ice volume transport is calculated by following the method Sumata et al. (2022) used for the sea ice flux calculation, but we compute it from the 5-day mean output using the ocean model ANHA12:

The sea ice volume transport:

$$T_{ICE} = \sum_{i=1}^n v_i c_i h_i x_i$$

where v_i is the cross-section ice drift velocity at each model grid cell; c_i is the sea ice concentration at each model grid cell; h_i is the sea ice thickness; x_i is the length of each grid cell along the section; n is the number of grid cells in the cross section.

The volume, freshwater and heat transports could reflect the amount of seawater, freshwater, and heat exchanges in the coupled ocean-sea ice model, respectively. The volume transport depends on the cross-strait velocity and section area. The calculations for the volume transport and heat transport can be found in (Fu et al. 2023). The freshwater transport derives from the volume transport with the salinity at each model grid cell being considered. Freshwater transport is equivalent to zero-salinity water flux that is added to

or deducted from the volume transport in reference salinity to reach the sample salinity.

The freshwater transport:

$$T_{FW} = \sum_{i=1}^n v_i A_i \left(\frac{S_{ref} - S_i}{S_{ref}} \right)$$

where v_i is the cross-strait seawater velocity at each model grid cell, A_i is the area of the single model grid cell, n is the number of grid cells in the cross section; S_i is the seawater salinity at each grid cell, S_{ref} is the reference salinity (equals to 34.8) (Wang et al. 2023);

2.3 Eddy energetics estimates

The current velocity at a given time can be split into the mean state and the variations from the mean state ($u = \bar{u} + u'$, $v = \bar{v} + v'$). The Total Kinetic Energy (TKE) is the sum of the Mean Kinetic Energy (MKE) and the time-varying Eddy Kinetic Energy (EKE) (Wang et al. 2020). The MKE is the energy related to the mean current while the EKE is the energy attributed to the mesoscale eddy and filament processes.

$$TKE = \frac{1}{2}(u^2 + v^2)$$

$$MKE = \frac{1}{2}(\bar{u}^2 + \bar{v}^2)$$

$$EKE = \frac{1}{2}(\overline{u'^2} + \overline{v'^2}) = \frac{1}{2}(\overline{u^2 + v^2} - \bar{u}^2 - \bar{v}^2)$$

where u and v represent the zonal and meridional velocity in the model field, respectively; \bar{u} and \bar{v} correspond to the time-mean velocity components and are calculated over 2008–2019; u' and v' correspond to the time-varying velocity components.

3 Observational datasets

3.1 Transport data for model evaluation

Three instrument arrays are employed to document the warm and saline AW inflows to the Nordic Seas across the Greenland Scotland Ridge (GSR), including the Iceland inflow array north of Iceland (1 in Figure S1), the Faroe Current array north of the Faroe Island (2 in Figure S1), and the Faroe–Shetland Channel inflow array in the Faroe–Shetland Channel (3 in Figure S1). The Iceland inflow array is a meridional section located at 21.5° W spanning from 66.9° N to 67.25° N with three moorings. The available transport data at this array starts from October 1994 to July 2016 with

monthly volume flux (plotted in Figure S6a). The current meters were deployed until 2009 to measure temperature and current velocity and then were replaced by Acoustic Doppler Current Profilers (ADCPs). The current meters were of the Aanderaa RCM7 type, and they recorded temperature and speed at the depths of 80 m and 150 m (See their Fig. 2 from Jónsson and Valdimarsson (2012)). More details about this array can be found in Jónsson and Valdimarsson (2012). The Faroe Current array is a combination of the Conductivity, temperature, depth (CTD) section and the ADCPs mooring

sites. The bottom temperature observations measured by the ADCP temperature sensor are also included in recent years for a more accurate representation of the AW water mass in the Faroe Current. The location of this mooring array is at 6.1° W spanning from 62.5° N to 64° N. The spatial resolution of the CTD stations is roughly 4 stations within 0.5° N and ADCPs are employed at seven different sites along the Faroe Current array from 62.70° N to 63.27° N (See their Fig. 1 and Table 1 from Hansen et al. (2015)). The time span of the transport measurements covers from January 1993

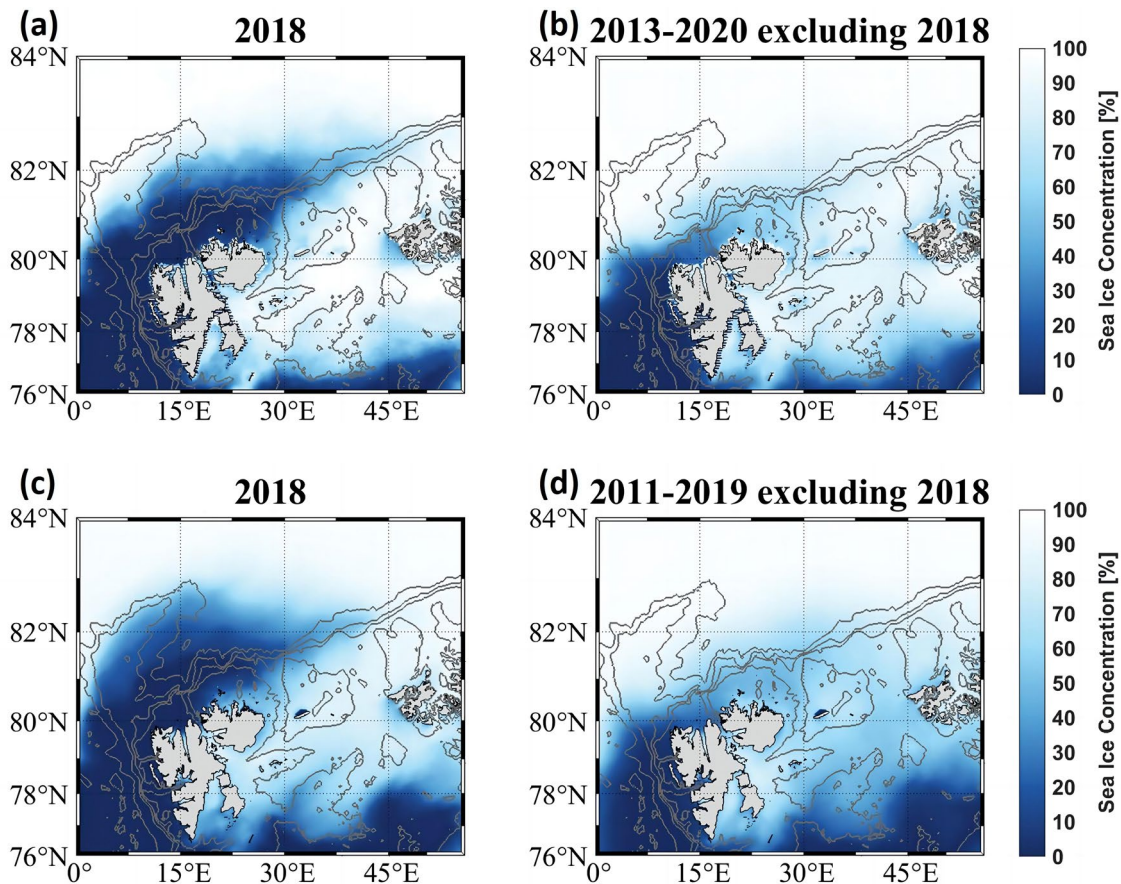


Fig. 2 Observed sea ice concentration (%) averaged over February–April from AMSR2 **a** in 2018; **b** 2013–2020 mean excluding 2018; Modelled sea ice concentration (%) averaged over February–April from ANHA12 **c** in 2018; **d** 2011–2019 mean excluding 2018

Table 1 The long-term mean of the AW inflow volume transport (unit: Sv; 1 Sv = 10⁶ m³/s) for each branch across the GSR from the observations and the ANHA12. I-Inflow: (Jónsson and Valdimarsson 2012); IF-Inflow: (Hansen et al 2015); FSC-Inflow: (Berx et al 2013)

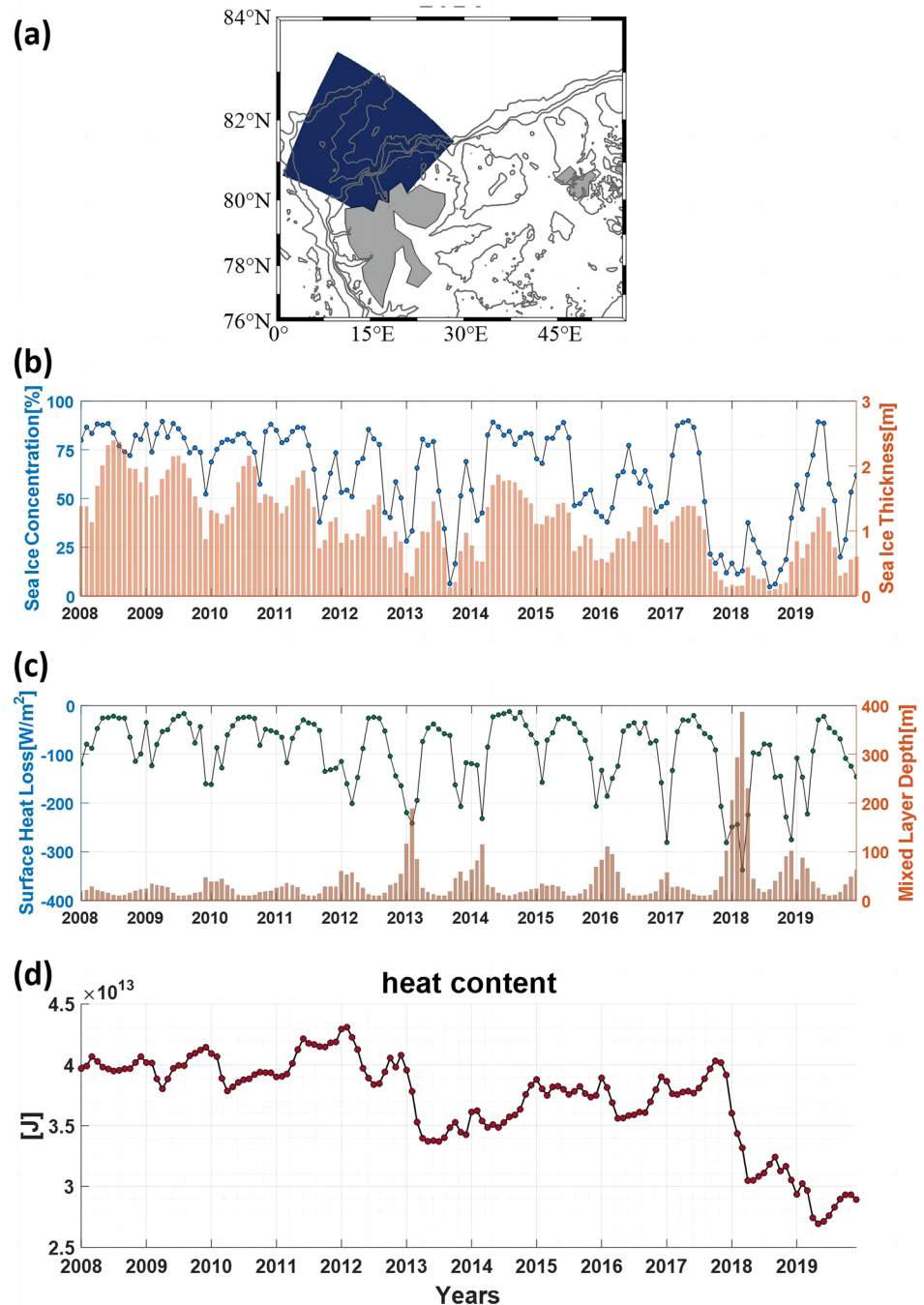
AW inflows	Observations		ANHA12	
	Periods	Mean volume transport (Sv)	Periods	Mean volume transport (Sv)
I-Inflow	1994.10–2016.07	0.88 ± 0.02	2002.01–2019.12	0.86 ± 0.02
IF-Inflow	1993.01–2017.04	3.82 ± 0.03	2002.01–2019.12	2.77 ± 0.04
FSC-Inflow	1993.01–2017.11	2.73 ± 0.06	2002.01–2019.12	3.29 ± 0.05
Total		7.43 ± 0.11		6.92 ± 0.07

Note that the results are nearly similar when comparing them using the overlapped observational and modelled time series

to April 2017 (plotted in Figure S6a). See more information in Hansen et al. (2015). The Faroe–Shetland Channel inflow array consists of CTD hydrographic sections to collect the temperature and salinity of the water mass and the ADCPs moored along the section to monitor the current velocity. This array measurement is supplemented with satellite altimetry observations which have been calibrated to provide a better estimate of the AW volume transport. The CTD section has typically been occupied six times a year with a decent monthly spread, although there have been no

occupations in January and only a handful in March–April and July–August (Berx et al. 2013). This array lies between latitudes 60.2° N and 61° N and longitudes 4° W and 5.844° W with 15 CTD stations and 9 ADCP mooring sites (See their Fig. 3 from Berx et al. (2013)). The transport data for this array begins in January 1993 and throughout November 2017 (plotted in Figure S6a). Berx et al. (2013) have a more detailed description of this array. All the transport data from these three arrays are provided by the contributing institutes of Faroe Islands University of Hamburg (UHAM),

Fig. 3 **a** study region north of Svalbard. **b** monthly averaged sea ice concentration (line graph; %) and sea ice thickness (bar; m) from 2008 to 2019 integrated over the study region from ANHA12. **c** monthly averaged surface heat loss (line graph; W/m^2) and mixed layer depth (bar; m) from 2008 to 2019 integrated over the study region from ANHA12. **d** monthly averaged heat content integrated over the top 1000 m water column referenced to 0°C over 2008–2019 from ANHA12



Hafrannsóknastofnun Marine and Freshwater Research Institute (MFRI), and Marine Scotland Science (MSS), and were downloaded from this site (<http://www.oceansites.org/tma/gsr.html>).

3.2 Sea ice concentration

Daily averaged sea ice concentration is derived from passive microwave remote sensing data of the sensor AMSR2 (Advanced Microwave Scanning Radiometer 2) on the JAXA satellite GCOM-W1, applying the ARTIST Sea Ice (ASI) algorithm. The AMSR2 sea ice concentration dataset is provided by the University of Bremen, Institute of Environmental Physics, available at <https://seaice.uni-bremen.de>. The data are gridded with 6.25 km resolution on a polar stereographic grid covering the whole Arctic Ocean (size: 1216 * 1792 pixels). The AMSR2 sea ice product implements the ASI algorithm on the NASA satellite Aqua and covers from 2 July 2012 until today. More details and descriptions are introduced in the ASI User Tutorial (https://seaice.uni-bremen.de/fileadmin/user_upload/ASIuserguide.pdf) (Melsheimer and Spreen 2019). In this study, the daily AMSR2 sea ice concentration data over February to April from 2013 to 2020 near the Svalbard region (Latitudes: 76–84° N; Longitudes: 0–56° E) are utilized for demonstration and analysis.

4 Model evaluation

As the northern end of the AMOC, the Atlantic Water (AW) flows into the Nordic Seas over the Greenland Scotland Ridge (GSR) in three branches (Figure S1), listed from north to south: North Icelandic Irminger Current (I-inflow), Faroe Current (IF-inflow), and Faroe–Shetland Channel Current (FSC-inflow). We consider three sections in accord with the mooring arrays that capture these three branches. Using ANHA12, we examine how the model performs in simulating the AW by comparing the modelled AW with the observations regarding the thermohaline structure, long-term mean, and seasonal and interannual variability of the AW transport.

The hydrographic conditions of the I-inflow are presented by the current meters in May 2000 from Jónsson and Valdimarsson (2012) (See their Fig. 2). Taking into account that our model simulation integration spans 2002–2021 and the model spin-up in the first two years, we choose the section plots in May 2004 from ANHA12 for comparison (Figure S2). The observed AW has a temperature core of over 5 °C sitting above the Icelandic shelf between the depth of 50–100 m. This is accompanied by a salinity core of over 35 PSU at an almost overlapping location. The modelled AW nicely depicts the temperature core over a similar

depth range despite having a higher maximum temperature of ~6 °C. The modelled salinity core also lies over the Icelandic shelf while the water mass saltier than 35 PSU occupies a larger area in the section plot. Fresher water (< 34.8 PSU) is found at the north of the section in the upper ocean of 50 m in both the observation and model.

The temperature and salinity of the IF-inflow are shown from the observations (averaged over 1993–2013) from Hansen et al. (2015) (See their Fig. 6a, c) and ANHA12 (averaged over 2004–2013) (Figure S3). The warm (~8 °C) and saline (~35.2 PSU) AW cores consistently appear over the Faroe slope from the CTD sections. The observed AW is mainly situated at the top 400 m of the water column and gradually becomes cooler and fresher further away from the temperature and salinity core. These features are well simulated from the ANHA12.

The thermohaline structure of the FSC-inflow is shown from the observations (averaged over 1995–2009) from Berx et al. (2013) (See their Fig. 4) and ANHA12 (averaged over 2004–2009) (Figure S4). The water mass is warm and saline in the upper layer of the channel. The observed AW core is located over the shelf of the Shetland side, with a temperature core greater than 10 °C and a salinity core greater than 35.35 PSU. The modelled AW presents the core at the same location with similar characteristics, but there is a larger amount of warm water of over 10 °C and saltier water of over 35.35 PSU at the core. The observed isotherm of 5 °C and isohaline of 35.2 PSU are located roughly between 300 and 500 m and reach slightly deeper on the Shetland side. This is also indicated in the model simulation. The model simulation demonstrates generally good agreement on these characteristics with the observational mooring arrays. Overall, the model has a decent performance in simulating the thermohaline structure of the AW inflows across the GSR, at the same time, it also shows a weakly warmer and saltier bias.

Based on the thermohaline structure, we define the AW inflows using different temperature and salinity constraints (I-inflow: $T > 3$ °C (Jónsson and Valdimarsson 2012); IF-inflow: $T > 4$ °C & $S > 35$ PSU (Hansen et al. 2015); FSC-inflow: $T > 5$ °C (Berx et al. 2013)) and calculate their volume transport through the corresponding sections. These definitions are derived to be consistent or close to various observational definitions. As we move from the more northerly to the more southerly sections, the lower bound for AW warms. The long-term mean of the AW volume transport for each inflow and the total transport are listed in Table 1. The mean modelled and observational I-inflow volume transport are nearly equivalent with a value of close to 0.9 Sv. The mean modelled IF-inflow (2.77 ± 0.04 Sv) is about 1 Sv lower than the mean observational IF-inflow (3.82 ± 0.03 Sv). However, the mean modelled FSC-inflow (3.29 ± 0.05 Sv) is higher than the mean observational

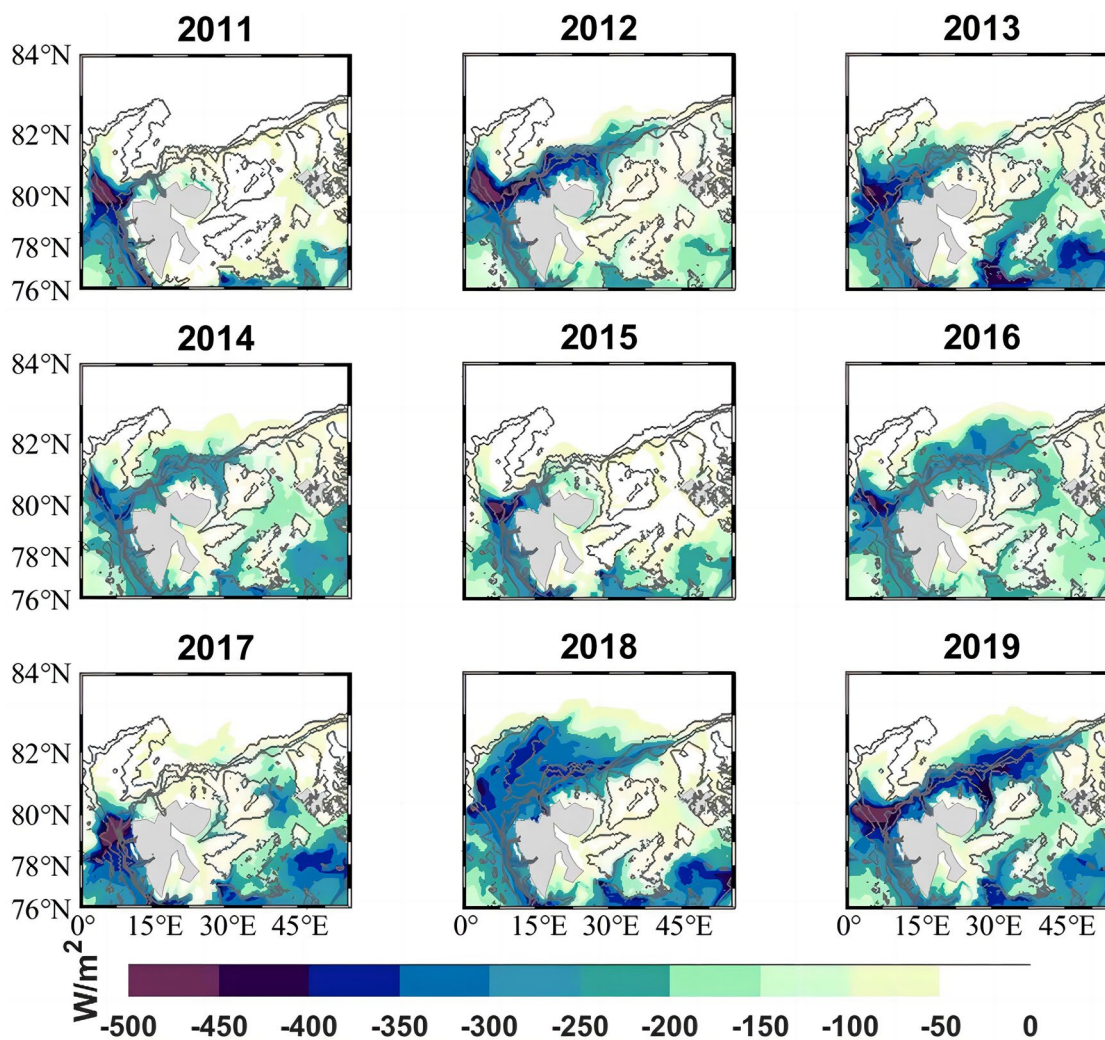


Fig. 4 Modelled surface heat loss (W/m^2) from ANHA12, averaged over February–April from 2011 to 2019

FSC-inflow (2.73 ± 0.06 Sv). This discrepancy might be ascribed to the fact that the model simulations are inclined to simulate warmer water than the observations. The lower modelled volume transport in IF-inflow can be explained by the presence of the salinity constraint. The total modelled AW transport is slightly less than the total observational transport (6.92 ± 0.07 Sv vs 7.43 ± 0.11 Sv), but they are comparable.

The seasonal cycles of the AW volume transport for each branch from ANHA12 and observations are then exhibited (Figure S5). The modelled seasonal cycles of the AW inflows well depict the observational seasonal cycles, although the relative strength between IF-inflow and FSC-inflow is not well presented in the model. The FSC-inflow has the most prominent seasonal cycle. It is anomalously eastward in the winter and westward in the summer referenced to the mean. It is consistent with the seasonal cycle of the cyclonic circulation in the Nordic Seas, which is governed by the strong

Icelandic Low in the winter. It is in phase with IF-inflow but out of phase with I-inflow. The interannual variability of the AW volume transport for each branch from ANHA12 (2002–2019) and observations (1993–2017) is shown in Figure S6. Each modelled AW branch is on a very similar scale as the observational ones. The interannual variability of I-inflow and FSC-inflow shares decent similarity between ANHA12 and observations from 2004 to 2015 with a correlation coefficient of 0.55 for the I-inflow and 0.51 for the FSC-inflow. In contrast, the correlation coefficient for the IF-inflow is only 0.24. There is an outstanding spike at the end of 2015 in FSC-inflow and this feature has been captured by both the observational and the modelled time series. Therefore, ANHA12 has relatively good simulation performance in terms of AW volume transport as well. ANHA12 has also been applied previously to present the Denmark Strait Overflow Water in February along the sections Látrabjarg and Kögur on the continental Icelandic shelf, and the model well

illustrates the overall structure of the water column along these two sections (García-Quintana et al. 2021; see their Fig. 2). It also well captured the observed reversal of Davis Strait net transport toward the Arctic Ocean at the end of 2010 (Myers et al. 2021; see their Fig. 1). A similar model evaluation conducted using ANHA12 concerning the AW inflows at Fram Strait and the Barents Sea Opening also supports the feasibility of its further application (Fu et al. 2023).

5 Results

5.1 Exceptional sea ice loss in the winter of 2018

It was identified in Athanase et al. (2020) that there is an exceptional sea ice retreat over the northern Yermak Plateau with the deepest Mixed Layer Depth (MLD) in the winter of 2018 using the Mercator 1/12° system. Averaging over the winter months (Feb.–April, when the largest MLD was observed in ANHA12) each year from 2013 to 2020, the observational sea ice concentration from the AMSR2 satellite record confirms that there is a significant sea ice cover reduction north of Svalbard in 2018 compared to the past decade (Figure S7). This feature has also been captured by ANHA12 of the same model resolution with a larger area of open water extending towards the northern Yermak Plateau, compared to observations (Figure S8). Similarly, ANHA12 shows thin and even absent sea ice (less than 1.25 m) in this same region in the winter of 2018 (Figure S9). To highlight the difference, we show both the observational and modelled sea ice concentration in the region only in 2018 and a composite of the other years (Fig. 2). Other than extending towards the northern Yermak Plateau, the exceptional sea ice retreat in 2018 extends further to the east along the slope of the Eurasian Basin following the Fram Strait Branch Water (FSBW) pathway (Fig. 2).

Using ANHA12, we are able to study this phenomenon and the associated physical processes in a larger temporal context. We chose a study region that covers the north of Svalbard in the model field (Fig. 3a). The monthly averaged sea ice concentration and sea ice thickness from 2008 to 2019 integrated over the region are computed using ANHA12 (Fig. 3b), together with the monthly surface heat loss and MLD (Fig. 3c). At the beginning of 2018, the substantial heat loss, corresponding with the minimum sea ice concentration and thickness, causes the deep MLD. We remark that the sea ice cover reached its minimum starting in the last few months of 2017 and throughout the whole year of 2018. Without the insulating sea ice cover in 2018, more oceanic heat is lost to the atmosphere (Fig. 4). Over the past decade, in most years, the heat loss is mainly concentrated in the northwest of Svalbard and along the FSBW pathway near the coast of Svalbard. The given year, 2018,

is the only year with a great heat loss to the atmosphere over the whole Yermak Plateau with a shift of the region of maximum loss to the Yermak Plateau. The surface heat loss is estimated to be $\sim 350 \text{ W/m}^2$ in the area without the sea ice north of Svalbard (Fig. 4). The open water condition allows intense winter convection, causing the averaged MLD to be over 300 m depth over north of Svalbard (Fig. 3c) and the maximum MLD to be over 600 m depth (Fig. 5) in 2018. In comparison, the MLD in other years is typically less than 70 m depth.

As shown in the monthly MLD time series in Fig. 3, there is the second-largest MLD peak in the winter of 2013. It is also indicated in the spatial MLD plot in Fig. 5 with a slightly deeper MLD along the FSBW pathway near the north of Svalbard compared to the other years except 2018. The MLD in 2013 does not reach the same magnitude and time span as the one in 2018, because the low sea ice cover does not last for a long period and the heat loss is not as significant as the one in 2018. Despite this, by calculating the heat content integrated over the top 1000 m water column referenced to 0 °C (Fig. 3d), we reveal two apparent heat content reductions in this region in both 2013 and 2018, from ~ 40 to ~ 34 TJ in 2013 and a larger drop from ~ 40 to ~ 30 TJ in 2018. These two significant heat content reductions in large parts contribute to the total heat content loss over the last decade. By the end of 2019, the total heat content over the north of Svalbard is below 30 TJ. The running correlation between sea ice concentration and surface heat loss over the time length of 13 months is computed from 2008 to 2019 (Figure S10). These two aspects have shown a positive correlation over most of the integration time, implying a greater heat loss that comes with low sea ice concentration. Note that a greater heat loss presents as a lower value in our calculation with a negative sign. However, the correlation became negative in 2018 when the sea ice cover was minimum in the north of Svalbard. This could be explained by wind-induced motion that causes the re-import of sea ice to the region on account of the thinner and fracturing sea ice in the vicinity of the region (Ivanov et al. 2016).

5.2 Mechanical mechanism: wind effect

Winds can modulate the sea ice motion, and the favorable winds could push ice offshore from Svalbard and expose direct contact with the relatively warm upper ocean and the atmosphere in winter (Ivanov et al. 2016; Lundesgaard et al. 2022). Athanase et al. (2020) explored the role of winds during the 2018 event and found the anomalously southwest wind stress component that is favorable to moving the sea ice out of the region (See their Fig. 9b). Our model study confirms the crucial role of winds in reducing the sea ice by dissecting the wind stress, which is derived from a different reanalysis-based forcing field (CGRF dataset). The

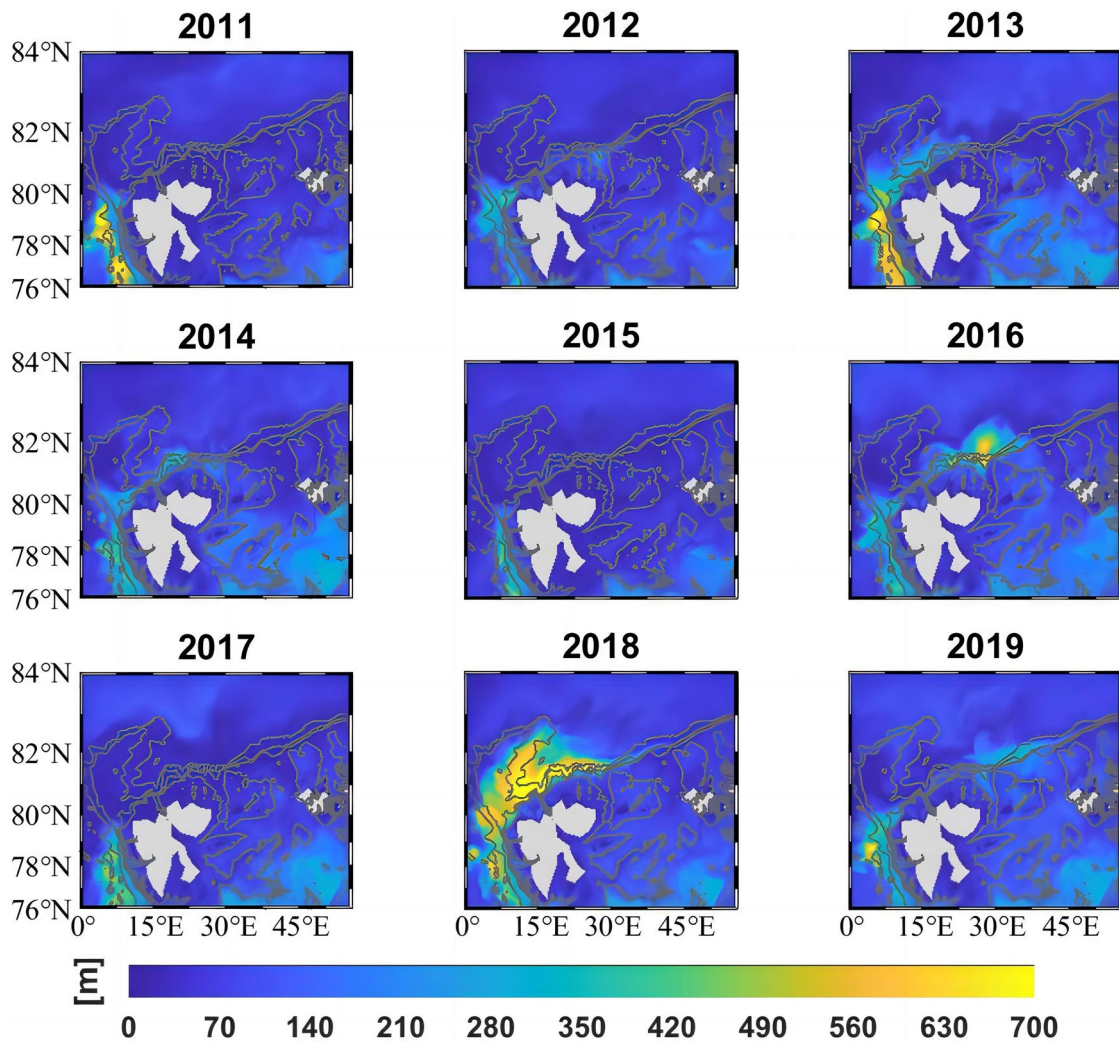


Fig. 5 Modelled mixed layer depth (m) from ANHA12, averaged over February–April from 2011 to 2019

anomalous wind prior to the event at the end of 2017 points to the southwest in the model field. It is composed of the negative zonal wind stress (reaching $\sim 0.05 \text{ N/m}^2$ to the west) combined with more strongly negative meridional wind stress (reaching $\sim 0.12 \text{ N/m}^2$ to the south) (not shown). The resulting Ekman transport forces the northwestward offshore sea ice movement. Prior to the deep winter convection in 2018, the sea ice north of Svalbard had begun to decline rapidly (Fig. 3b). Hence, the observed and modelled sea ice anomalies and thereafter the deep winter convection are initiated by the wind forcing that functions as a driving force to establish an open water condition north of Svalbard.

5.3 Thermodynamic mechanism: AW transport

Having explored the mechanical processes caused by winds, we then relate the sea ice reduction to the possible thermodynamic contribution associated with the heat

brought by inflowing AW. The AW is defined as a water mass with a temperature greater than 2°C and a salinity greater than 35 PSU, adapted from Beszczynska-Möller et al. (2012) who used $T > 2^\circ \text{C}$ without salinity constraint. By calculating the AW volume and heat transport through Fram Strait, we notice an apparent warm AW signal spike in 2017 (Fig. 6). The AW volume transport reaches its maximum of $\sim 5.5 \text{ Sv}$ in 2017, accompanied by a peak of the AW heat transport of $\sim 110 \text{ TW}$. To investigate how much of the heat will be advected into this region, we present the temperature field over the AW layer of 200–600 m averaged over August–October in 2017 before other processes (i.e. substantial heat loss to the atmosphere during the event) kick in (Fig. 7). Compared with the mean state over 2008–2019, warmer AW of $\sim 4^\circ \text{C}$ is found to enter the Yermak Plateau and propagate along the FSBC pathway north of Svalbard. The whole Yermak Plateau region exhibits a generally warmer status than the mean state.

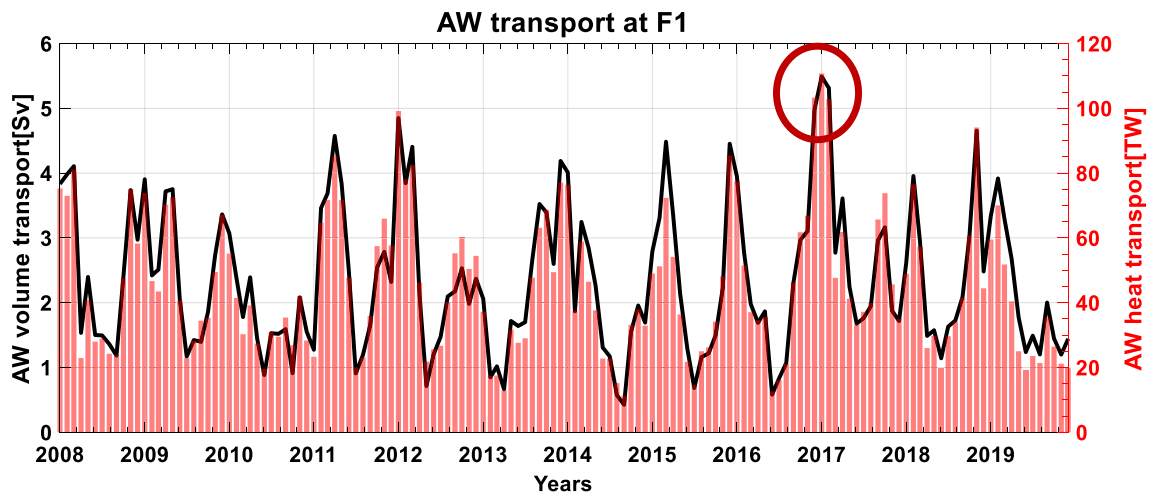


Fig. 6 Monthly averaged Atlantic Water (AW) volume (line; Sv) and heat (bar; TW) transport through Fram Strait (F1, shown in Fig. 1) from 2008 to 2019. The AW definition is $T > 2\text{ }^{\circ}\text{C}$, $S > 35\text{ PSU}$. The positive value represents the AW flowing northward into the Arctic Ocean

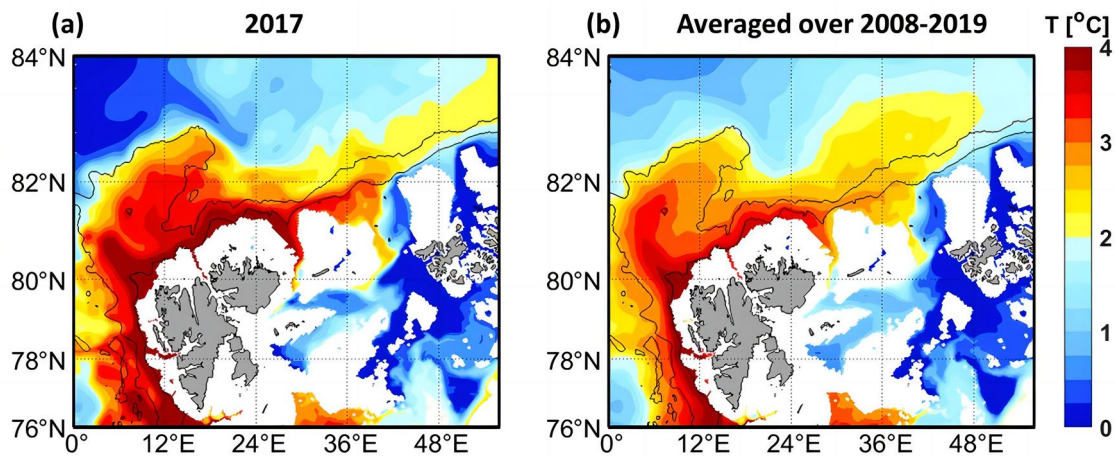


Fig. 7 Mean temperature fields over the depth of 200–600 m averaged over August–October in 2017 (a) and during 2008–2019 (b) from ANHA12 simulation

The additional amount of heat carried by the AW eventually contributes to the apparent sea ice reduction during the event. To demonstrate our point of enhanced AW heat results in the sea ice melting, we computed the oceanic heat flux at the sea ice base north of Svalbard (Figure S11). The spike in the oceanic heat flux at the beginning of 2017 reduces the sea ice thickness, showing the direct link between the excess AW heat and thinning sea ice. The heat flux to sea ice during the deep winter convection in 2018 is significantly large, of $\sim 100\text{ W/m}^2$, despite the anomalously thin/missing ice in this region. This attests that while the favorable winds create open water conditions before the event, the melting of sea ice during the event is attributed to the upward AW heat. Therefore, the AW through Fram Strait and the subsequent warmer ocean state in the AW

layer plays a crucial role in preconditioning the region for deep winter convection.

5.4 AW properties change and mesoscale eddy activity

To understand the hydrographic properties of the AW along the water column over the Yermak Plateau, we compute section plots at model sections F2, F3, and F4, showing the temperature, salinity, and cross-section velocity during the event (February–April in 2018) and the long-term average over 2008–2019 (Figs. 8, S12, S13). Our three sections well document the property changes of the AW as it propagates eastward along the north of Svalbard over the long term and during the event. The long-term AW state over 2008–2019

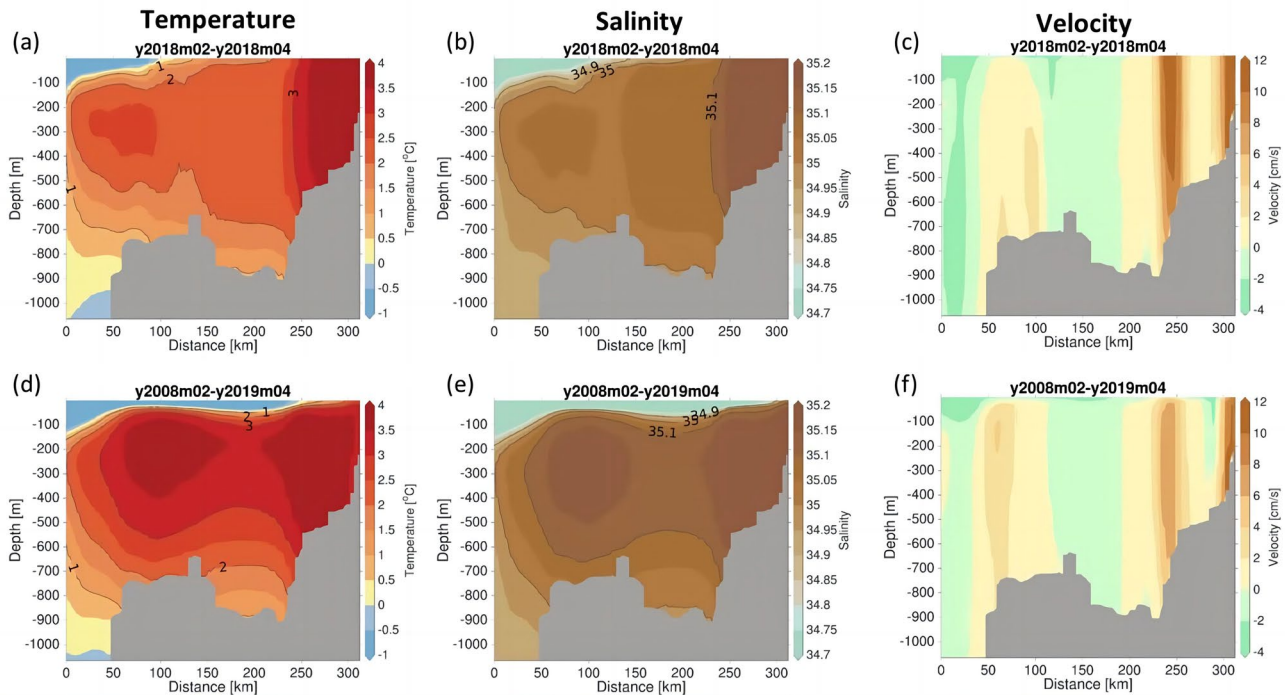


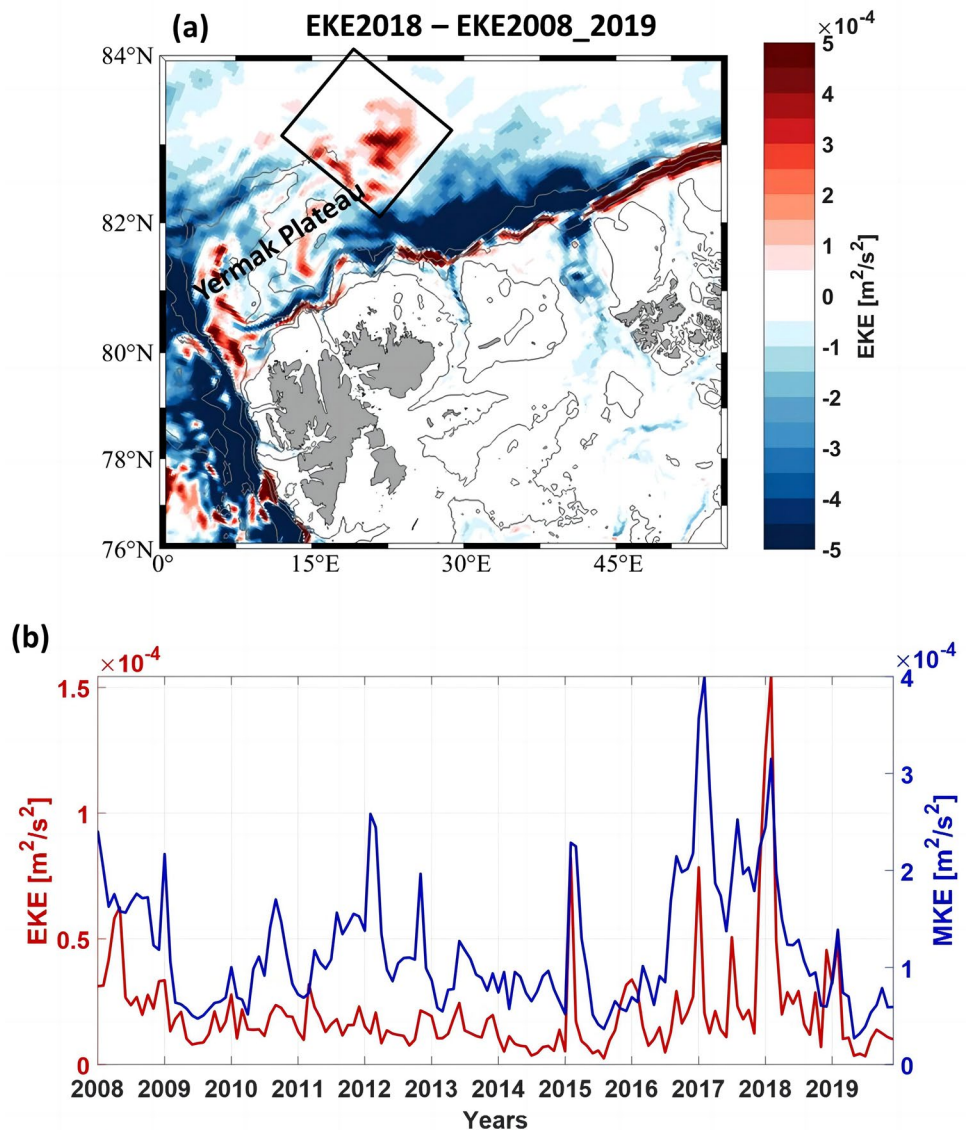
Fig. 8 Section plots in section F2 averaged over February–April in 2018 (a, b, c) and averaged over February–April for 2008–2019 (d, e, f). (a, d) mean temperature T ($^{\circ}\text{C}$). (b, e) salinity S (PSU). (c, f) normal to cross-section velocity. The velocity is positive towards the

Arctic Ocean. The x-axis shows the distance in kilometres and the y-axis shows the ocean depth in metres. See the section location in Fig. 1, marked in blue

in section F2 has exhibited two AW cores with temperatures of ~ 3.5 $^{\circ}\text{C}$ and salinities of ~ 35.15 PSU (Fig. 8d, e). The velocity fields in F2 also indicate three AW inflows with the strongest being the Yermak Pass Branch that flows across the Yermak Plateau (Fig. 8f). The long-term AW becomes cooled and freshened as it reaches section F3. There is only one clear AW core with a temperature of ~ 3 $^{\circ}\text{C}$ and a salinity of ~ 35.1 PSU (Figure S12d, e). The cooling and freshening effect continues when it arrives at F4. The area of the AW core has shrunk and its location is limited to be over the slope (Figure S13d, e). During the event in F2, the deep convection mixes the cold and fresh surface water with warm and saline AW, making the water column less stratified (Fig. 8a, b). While the temperature and salinity of the AW core near shore remain almost unchanged, the one away from the shore gets cooled and freshened during the winter of 2018, changing from ~ 3.5 to ~ 2.5 $^{\circ}\text{C}$ for temperature and from ~ 35.15 to ~ 35.05 PSU for salinity (Fig. 8a, b, d, e). Though using a different transect across the Yermak Plateau at 81.5°N , the study from Athanase et al. (2020) showed a drastic AW property change at the AW layer between the onset and cessation of the deep convection in the winter of 2018. The temperature of the AW was above 3 $^{\circ}\text{C}$ at the end of 2017 and cooled to 1.5 – 2.5 $^{\circ}\text{C}$ at the end of March and the salinity of the AW changed from ~ 35.2 PSU to be in the range of 35.05 – 35.2 PSU. The thermohaline structure

in section F3 is also weakly stratified and the thermohaline properties of the water mass are more consistent vertically through the water column (Figure S12a, b). The AW core away from the shore disappears and the one near the shore experiences a decrease in both temperature (from ~ 3.5 $^{\circ}\text{C}$ in F2 to ~ 3 $^{\circ}\text{C}$ in F3) and salinity (from ~ 35.15 PSU in F2 to ~ 35.1 PSU in F3). The AW during the event is further cooled and freshened downstream along the FSBW pathway in section F4. The temperature and salinity of the AW core over the slope in F4 are ~ 2 $^{\circ}\text{C}$ and 35 PSU, respectively (Figure S13a, b). The convective mixing area does not extend to section F4 (Figure S13a, b, Fig. 5). Nevertheless, we observe a second AW core at the northern end of the section with temperature cores of > 2 $^{\circ}\text{C}$ and salinity cores of > 35 PSU. The dipolar flow around the 50 km marking suggests enhanced eddy fluxes during the event. The enhanced eddy fluxes are responsible for the AW return flows at section F4 and accelerate the exchange of heat away from the AW core along the main FSBW pathway. To confirm this, we plot the eddy kinetic energy (EKE) difference between during the event and the long-term mean over 2008–2019 (Fig. 9a). The plot presents an enhanced mesoscale eddy activity appearing on the boundary of the Yermak Plateau, especially to the east during 2018. By selecting the region east of the Yermak Plateau, which covers the area of the AW return flows, we compute EKE and MKE averaged over 200–600 m in

Fig. 9 **a** Eddy kinetic energy averaged over February–April in 2018 minus eddy kinetic energy averaged over February–April for 2008–2019 (m^2/s^2); the integrating region east of the Yermak Plateau for the calculation of kinetic energy is indicated by the black box. **b** time series of eddy kinetic energy (EKE; red line) and mean kinetic energy (MKE; blue line) averaged over 200–600 m from 2008 to 2019



the AW layer (Fig. 9b). We detect an extremely high EKE during the event, peaking at slightly over $1.5 \times 10^{-4} \text{ m}^2/\text{s}^2$ with the second highest peak of MKE ($\sim 3.0 \times 10^{-4} \text{ m}^2/\text{s}^2$) throughout the time series. The variability of EKE and MKE is well correlated but not necessarily consistent with each other. As Zhao et al. (2014) suggest that numerous eddies are found in the Arctic halocline, we implement a similar analysis but now averaged over 100–200 m (Figure S14). The EKE maximum during the 2018 event stands out in this new time series, reaching at $2.5 \times 10^{-4} \text{ m}^2/\text{s}^2$, implying enhanced mesoscale eddy activity in the Arctic halocline.

5.5 Sea ice flux through Fram Strait in 2018

Another impact of this event is its potential linkage to the unprecedented low sea ice export out of the Arctic Ocean in 2018, shown in both the observations (Sumata et al. 2022;

see their Fig. 3) and ANHA12 (Fig. 10a). Though using the same method for sea ice flux calculation as Sumata et al. (2022), we expand the section (Flce, spanning from -18° W to 12° E at 78.8° N) to connect East Greenland to Svalbard for documenting all the sea ice export out of the Arctic Ocean through Fram Strait in the model. The southward sea ice volume flux has exhibited a declining trend from $\sim 130 \text{ km}^3/\text{month}$ to $\sim 40 \text{ km}^3/\text{month}$ over 2008–2019, with a minimum yearly flux of $\sim 35 \text{ km}^3/\text{month}$ in 2018. This number is close to the annual mean volume flux of $\sim 40 \text{ km}^3/\text{month}$ computed from Upward Looking Sonars (ULSs) and Ice Profiling Sonars (IPs) (Sumata et al. 2022). We examine this relationship by comparing the sea ice drift superimposed on a map of the sea ice thickness in the Arctic between the event in 2018 and the long-term average over 2008–2019 (Fig. 10b, c). The long-term averaged sea ice congregates along the northern edge of the CAA with the

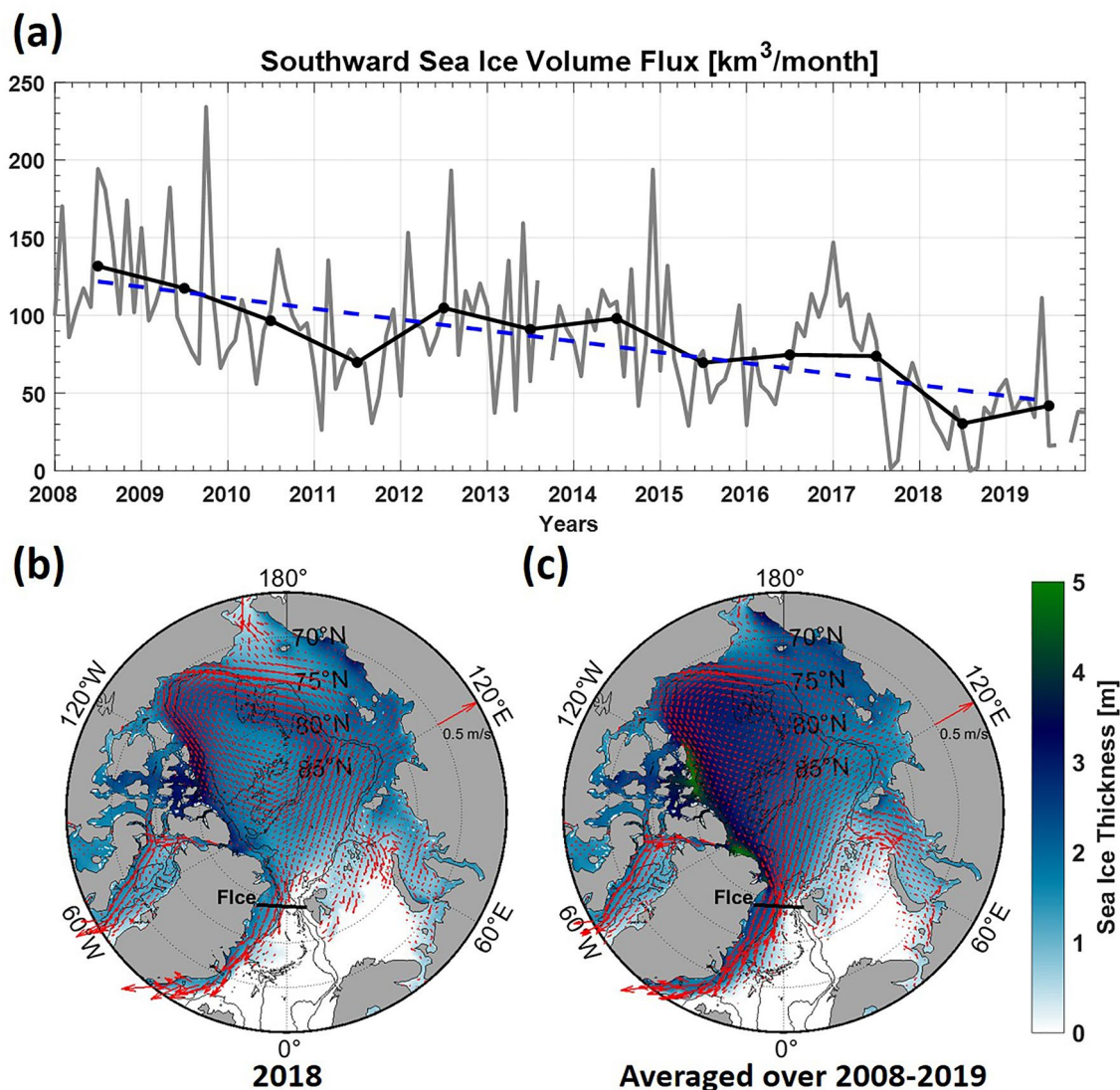


Fig. 10 **a** Monthly (grey line) and annual (black line) averaged southward sea ice volume flux (km³/month) through section FIce (shown in **(b, c)**) from 2008 to 2019. The trend is depicted using the linear least square method (blue dashed line). The positive value indicates

the sea ice export out of the Arctic Ocean. **b** sea ice drift (red arrow; m/s) and sea ice thickness (colour; m) averaged over February–April in 2018. **c** Same as **(b)**, but for 2008–2019

sea ice thickness over 4 m (Fig. 10c). The sea ice primarily exits the Arctic Ocean on the west side of Fram Strait along with the East Greenland Current and eventually enters the North Atlantic Ocean. The strength of the sea ice export velocity out of the Fram Strait significantly reduces in 2018 relative to the long-term mean. Therefore, the minimum southward sea ice export is mainly induced by the reduced sea ice export velocity through Fram Strait and thinner sea ice transported by the Transpolar Drift. It can also be partly ascribed to the absence of sea ice over the Yermak Plateau which results in a very small amount of sea ice flux on the east side of Fram Strait during the event (Figs. 2, 10b). The southward freshwater flux through Fram Strait has also been

declining during recent years (Figure S15). The declining trend is indicated in Karpouzoglou et al. (2022) as well, see their Fig. 7. Together with a relatively low southward freshwater flux of ~160 km³/month, the minimum sea ice export in 2018 might be a potential negative freshwater anomaly to the Nordic seas and subpolar North Atlantic Ocean.

6 Discussion and conclusions

Focusing on the Yermak Plateau north of Svalbard (Fig. 1), we explore the exceptional sea ice reduction in 2018 compared to the rest of the years in the last decade. The

phenomenon was initially identified by Athanase et al. (2020) using the Mercator 1/12° ocean model, confirmed by the sea ice AMSR2 observation. This finding is supported by our study applying the ANHA12 ocean model simulation (Fig. 2). Our ANHA12 configuration is evaluated by comparing the mooring measurements and ANHA12 in terms of the thermohaline structure, the interannual and seasonal variability, as well as the long-term mean of the volume transport from three AW inflows across the Greenland Scotland Ridge (GSR) (Figure S1–6, Table 1). The AW volume and heat transport through Fram Strait were also evaluated by a previous model study using ANHA12 (Fu et al. 2023). The disappearance of sea ice north of Svalbard renders deep convection over the Yermak Plateau in 2018, leading to a significant heat content reduction of ~ 10 TJ (Fig. 3). Note that the amplitude of the winter deep convection is confined by the structure of the local ocean bottom bathymetry. The concept of deep convection here is relative to the mean state of the typical winter convection that occurs in this region (maximum MLD > 600 m in 2018 vs ~ 70 m in other years over the Yermak Plateau; Fig. 5). It has been proposed from several previous studies that the winter ice-free condition north of Svalbard was preconditioned by favorable wind-induced motion that pushes the sea ice out of the region and the higher water temperature in the AW layer. A large heat flux to the atmosphere and the subsequent deep convective mixing play a crucial role in maintaining the open ocean condition by entraining the warm AW from the AW layer and thereby bringing ocean heat to the surface (Ivanov et al. 2016; Koenig et al. 2017a, b; Lundesgaard et al. 2022; Athanase et al. 2020). Our model study has not only more explicitly confirmed the two strongly suspected drivers of the favorable wind and the AW heat in the 2018 deep convection event, linking the additional heat north of Svalbard in the AW layer to the anomalous AW inflow through Fram Strait, but also extended the existing studies by probing the potential impacts and implications of the event.

The southwestward wind over the study region before the deep convection in 2018 suppresses the sea ice advection, which is in good agreement with Onarheim et al. (2014)'s finding that the southward component of the local wind can be accounted for the reduced sea ice in this region. Our study quantifies the wind effect by indicating the westward wind stress of ~ 0.05 N/m² and stronger southward wind stress of ~ 0.12 N/m² in our model field (not shown). The negative correlation between sea ice concentration and heat lost to the atmosphere also implies the wind-forced motion causing the re-import of sea ice after the deep convection (Figure S10). Our study specifically finds that water temperature averaged over August–October of 2017 prior to the deep convection north of Svalbard in the AW layer is generally higher than the mean state over 2008–2019, which has been ascribed to the anomalous heat carried by the AW through Fram Strait,

reaching its maximum of ~ 110 TW during the winter of 2017 (Figs. 6, 7). The warm pulse of the AW through Fram Strait can be an indicator of the negative sea ice anomalies north of Svalbard (Ivanov et al. 2012, 2016), even though its impact alone might not be able to set the sea ice variability on the interannual time scale (Lundesgaard et al. 2021), indicating the mutual effects of winds and AW heat at play in the 2018 event. The maximum AW volume and heat transport are transmitted from the AW peak at the end of 2015 in the Faroe–Shetland Channel Current (FSC-inflow) over the GSR, diagnosed by both the observational and modelled transport time series (Figure S6). The maximum AW peak occurs concurrently with the positive highest annual mean of the Arctic Oscillation (AO) index in 2015, which manifests itself as a trough of low pressure over the Arctic Ocean. The resulting strong westerly winds might act as a driving force accelerating the FSC-inflow. The apparent warm AW signal in 2017 brings more heat into the AW layer of the study region and enhances the sea ice melt initially through upward heat transfer. With the weakening/missing capping effect from sea ice cover north of Svalbard driven by the wind forcing, substantial heat loss due to wintertime cooling produces denser water, triggering deep convection. The vertical overturning and mixing weaken the water stratification but strengthen the rate of heat advection and dissipation, and thus contribute to the sea ice melting to a much greater extent (Polyakov et al. 2017). These processes form a positive feedback loop that leads to the unprecedented sea ice reduction over the Yermak Plateau in 2018.

One significant impact of the deep convection event in 2018 is the modification of the AW hydrographic properties (Athanase et al. 2020). By drawing three model sections that are nearly perpendicular to the continental slope north of Svalbard, our section plots provide a more detailed description of how the AW core properties alter during the event along its eastward propagation pathway (Figs. 8, S12, and S13). Similar to the AW over the whole study period, the AW during the event still gets cooled and freshened along its pathway, as the temperature and salinity of the AW core of ~ 3.5 °C and ~ 35.15 PSU near the shore in section F2 decreases to of ~ 2 °C and ~ 35 PSU in F4. A second AW core featuring the dipolar flow in F4 indicates the active participation of eddies, which are a key attribute to the lateral AW ventilation into the interior Eurasian Basin (Figure S13). Another significant impact of the 2018 event is that it corresponds to enhanced mesoscale eddy activity on the boundary of the Yermak Plateau, especially to the east (Fig. 9a). The enhanced mesoscale eddy activity is suggested by the strikingly high Eddy Kinetic Energy (EKE) averaged over the eastern region to the Yermak Plateau, which appears in both the AW layer and Arctic halocline (Fig. 9b, Figure S14). The lateral mesoscale eddy fluxes represent an effective means of transporting warm and salty AW and releasing

the heat from the AW boundary current. The extremely high EKE might be the result of the mixed-layer instabilities induced by the drastic buoyancy gradients crossing the ice-edge meltwater fronts (Manucharyan and Thompson 2017). Since the eastern Yermak Plateau is situated at the Marginal Ice Zone (MIZ, Fig. 2), eddies in this region play a crucial role in interacting with sea ice and distorting the ice edge (Johannessen et al. 1987; Smith and Bird 1991). Cyclonic eddies can cause the convergence of sea ice, trapping and advecting it to the warmer surface waters; on the other hand, they transport AW heat in the mixed layer under the sea ice over the MIZ, significantly warming the ice-covered ocean and subsequently causing the expansion of the MIZ width (Johannessen et al. 1987; Manucharyan and Thompson 2017). Therefore, eddies in this region can also determine the MIZ by fracturing sea ice dynamically and melting sea ice thermodynamically. The exceptional sea ice loss north of Svalbard can partly contribute to the minimum southward sea ice volume flux through Fram Strait in 2018 (Fig. 10). Considering the southward freshwater flux through Fram Strait also being relatively low this year (Figure S15), it means less freshwater is transported to the Nordic Seas and then the northern Atlantic Ocean. This likely results in a salinity increase in the upper layer, dampens the water stratification, and potentially exerts a promoting effect on the transformation processes of the Atlantic Meridional Overturning Circulation (AMOC) in the North Atlantic.

The transformation of the AW due to the deep winter convection also potentially provides an additional source of water to the lower limb of the AMOC. Lozier et al. (2019) concluded that the AMOC variability in the subpolar North Atlantic is primarily dominated by the conversion of warm, salty and shallow AW to cold, fresh and denser deep waters in the Irminger and Iceland basins. Huang et al. (2020) later revealed that the wintertime deep water formation taking place in the interior of the Greenland basin supplies the densest portion of overflow waters across the GSR based on historical hydrographic data over 2005–2015 and satellite altimeter data. Our model study further suggests that deep convection sites, which play a role in the transformation loop of the AMOC, may have begun to exhibit a trend of moving northward into the Arctic Ocean as the sea ice retreats. More frequent convection events over the Yermak Plateau in recent years together with the anomalously 2018 deep convection from our study hints at the possibility of such an occurrence.

The Arctic Ocean has experienced drastic changes in recent decades. The Arctic has been warming nearly four times faster than the rest of the globe since 1979 and has shown the largest temperature change, the so-called “Arctic Amplification” (Rantanen et al. 2022). Guarino et al. (2020) also proposed a warming world and the possibility of an ice-free Arctic Ocean (less than 10^6 km²) in summer as early as

2030–2050. The link between the region of deep convection and the location of AMOC headwaters under a warming climate is investigated utilizing simulations from the climate models (Lique et al. 2018; Lique and Thomas 2018). The latitudinally northward migration of the deep convection region corresponds to the northward retreat of the winter sea ice edge that allows greater air-sea buoyancy fluxes to impact the Eurasian Basin. Since the mixed-layer subduction is the key process contributing significantly to the AMOC conversion, the northward migration of the deep convection sites indicates the northward shift of the AMOC headwaters. The region north of Svalbard is the most dominant region of the AMOC deep limb under the future warmer climate (Lique and Thomas 2018; See their Fig. 4). Our study exemplifies that more years of greater deep convection and extremely deep MLD can be anticipated as the Arctic Ocean is becoming seasonally ice-free with a trend of younger and thinner sea ice (Cavalieri and Parkinson 2012; Comiso 2012; Spreen et al. 2020; Timmermans and Marshall 2020). The deep convection sites for the AMOC are expected to move northward into the Arctic Ocean (Bretones et al. 2022) and the intermediate/deep water formation and circulation will accordingly change in the future warmer Arctic Ocean. This will have important implications for a wide range of ocean processes, including the heat and salt redistribution as well as nutrients and gases intake in the high-latitude ocean. Therefore, keeping track of anomalously deep convection events in the Arctic Ocean with ocean/climate models at higher resolutions is warranted to better understand the future ocean revolution.

Supplementary Information The online version contains supplementary material available at <https://doi.org/10.1007/s00382-023-07027-8>.

Acknowledgements We gratefully acknowledge the financial and logistic support of grants from the Natural Sciences and Engineering Research Council (NSERC) of Canada. These include a Discovery Grant (rgpin227438-09) awarded to P.G. Myers, and a Climate Change and Atmospheric Research Grant (VITALS - RGPCC 433898). We acknowledge the funding support from the Chinese Scholarship Council (student number: 202208180005). We are grateful to the NEMO development team and the Drakkar project for providing the model and continuous guidance. We would also like to thank G. Smith for the model atmospheric forcing fields, made available by Environment and Climate Change Canada (https://weather.gc.ca/grib/grib2_glb_25km_e.html). We thank Westgrid and Compute Canada for computational resources, where all model experiments were performed. We sincerely appreciate the two reviewers for their detailed and constructive comments on the previous version of this manuscript.

Author contributions CF was responsible for analyzing data, interpreting results, and writing the manuscript. PM helped with experiment design, and manuscript edits, as well as provided comments and feedback. Both authors read and approved the final manuscript.

Funding We received the financial and logistic support of grants from the Natural Sciences and Engineering Research Council (NSERC) of Canada. These include a Discovery Grant (rgpin227438-09) awarded to P.G. Myers, and a Climate Change and Atmospheric Research Grant (VITALS - RGPCC 433898). We also have funding support from the

Chinese Scholarship Council that has been awarded to C. Fu (student number: 202208180005).

Data availability The model code based on the NEMO model is available at <https://www.nemo-ocean.eu/> (last access: 28 May 2017, Madec, 2008). Details on the ANHA configuration used are available at <http://knossos.eas.ualberta.ca/anha/index.php> (last access: 8 September 2017), with files for the experiment used in this paper at <https://doi.org/https://doi.org/10.7939/DVN/5G0NGP>.

Declarations

Conflict of interest We declare that the authors have no competing interests as defined by Springer, or other interests that might be perceived to influence the results and/or discussion reported in this paper.

Ethical approval Not applicable.

Open Access This article is licensed under a Creative Commons Attribution 4.0 International License, which permits use, sharing, adaptation, distribution and reproduction in any medium or format, as long as you give appropriate credit to the original author(s) and the source, provide a link to the Creative Commons licence, and indicate if changes were made. The images or other third party material in this article are included in the article's Creative Commons licence, unless indicated otherwise in a credit line to the material. If material is not included in the article's Creative Commons licence and your intended use is not permitted by statutory regulation or exceeds the permitted use, you will need to obtain permission directly from the copyright holder. To view a copy of this licence, visit <http://creativecommons.org/licenses/by/4.0/>.

References

- Appen W-J, Schauer U, Hattermann T, Beszczynska-Möller A (2016) Seasonal cycle of mesoscale instability of the west spitsbergen current. *J Phys Oceanogr* 46(4):1231–1254. <https://doi.org/10.1175/jpo-d-15-0184.1>
- Athanase M, Sennéchaël N, Garric G, Koenig Z, Boles E, Provost C (2019) New hydrographic measurements of the upper arctic western Eurasian basin in 2017 reveal fresher mixed layer and shallower warm layer than 2005–2012 climatology. *J Geophys Res Oceans* 124(2):1091–1114. <https://doi.org/10.1029/2018jc014701>
- Athanase M, Provost C, Pérez-Hernández MD, Sennéchaël N, Bertoso C, Artana C, Garric G, Lellouche JM (2020) Atlantic water modification north of Svalbard in the mercator physical system from 2007 to 2020. *J Geophys Res Oceans* 125(10):1–26. <https://doi.org/10.1029/2020JC016463>
- Athanase M, Provost C, Artana C, Pérez-Hernández MD, Sennéchaël N, Bertoso C, Garric G, Lellouche J, Prandi P (2021) Changes in Atlantic water circulation patterns and volume transports north of Svalbard over the last 12 years (2008–2020). *J Geophys Res Oceans*. <https://doi.org/10.1029/2020jc016825>
- Berx B, Hansen B, Østerhus S, Larsen KM, Sherwin T, Jochumsen K (2013) Combining in situ measurements and altimetry to estimate volume, heat and salt transport variability through the Faroe–Shetland Channel. *Ocean Sci* 9(4):639–654. <https://doi.org/10.5194/os-9-639-2013>
- Beszczynska-Möller A, Fahrbach E, Schauer U, Hansen E (2012) Variability in Atlantic water temperature and transport at the entrance to the Arctic Ocean, 1997–2010. *ICES J Mar Sci* 69(5):852–863. <https://doi.org/10.1093/icesjms/fss056>
- Boyd TJ, D'Asaro EA (1994) Cooling of the west Spitsbergen current: wintertime observations west of Svalbard. *J Geophys Res* 99:C11. <https://doi.org/10.1029/94jc01824>
- Bretones A, Nisancioglu KH, Jensen MF, Brakstad A, Yang S (2022) Transient increase in Arctic deep-water formation and ocean circulation under sea ice retreat. *J Clim* 35(1):109–124. <https://doi.org/10.1175/JCLI-D-21-0152.1>
- Cavaliere DJ, Parkinson CL (2012) Arctic sea ice variability and trends, 1979–2010. *Cryosphere* 6(4):881–889. <https://doi.org/10.5194/tc-6-881-2012>
- Chatterjee S, Raj RP, Bertino L, Skagseth Ø, Ravichandran M, Johannessen OM (2018) Role of Greenland Sea Gyre circulation on atlantic water temperature variability in the Fram Strait. *Geophys Res Lett* 45(16):8399–8406. <https://doi.org/10.1029/2018GL079174>
- Cokelet ED, Tervalon N, Bellingham JG (2008) Hydrography of the west Spitsbergen current, Svalbard Branch: autumn 2001. *J Geophys Res Oceans*. <https://doi.org/10.1029/2007JC00415>
- Comiso JC (2012) Large decadal decline of the arctic multiyear ice cover. *J Clim* 25(4):1176–1193. <https://doi.org/10.1175/JCLI-D-11-00113.1>
- Crews L, Sundfjord A, Albretsen J, Hattermann T (2018) Mesoscale Eddy activity and transport in the Atlantic water inflow region north of Svalbard. *J Geophys Res Oceans* 123(1):201–215. <https://doi.org/10.1002/2017JC013198>
- Crews L, Sundfjord A, Hattermann T (2019) How the Yermak Pass branch regulates Atlantic water inflow to the Arctic ocean. *J Geophys Res Oceans* 124(1):267–280. <https://doi.org/10.1029/2018jc014476>
- Da Costa MV, Mercier H, Treguier AM (2005) Effects of the mixed layer time variability on kinematic subduction rate diagnostics. *J Phys Oceanogr* 35(4):427–443. <https://doi.org/10.1175/jpo2693.1>
- Fichefet T, Maqueda MAM (1997) Sensitivity of a global sea ice model to the treatment of ice thermodynamics and dynamics. *J Geophys Res Oceans* 102(C6):12609–12646. <https://doi.org/10.1029/97jc00480>
- Fu C, Pennelly C, Garcia-Quintana Y, Myers PG (2023) Pulses of cold Atlantic water in the Arctic ocean from an ocean model simulation. *J Geophys Res Oceans* 128(5):e2023JC019663. <https://doi.org/10.1029/2023JC019663>
- Garcia-Quintana Y, Grivault N, Hu X, Myers PG (2021) Dense water formation on the icelandic shelf and its contribution to the north Icelandic jet. *J Geophys Res Oceans* 126(8):1–22. <https://doi.org/10.1029/2020JC016951>
- Gascard J-C, Richez C, Rouault C (1995) New insights on large-scale oceanography in Fram Strait: the west Spitsbergen current. *Arctic Oceanogr Marg Ice Zones Cont Shelves* 49:131–182. <https://doi.org/10.1029/ce049p0131>
- Guarino M-V, Sime LC, Schröder D, Malmierca-Vallet I, Rosenblum E, Ringer M, Ridley J, Feltham D, Bitz C, Steig EJ, Wolff E, Stroeve J, Sellar A (2020) Sea-ice-free Arctic during the last interglacial supports fast future loss. *Nat Clim Chang* 10(10):928–932. <https://doi.org/10.1038/s41558-020-0865-2>
- Hansen B, Larsen KMH, Hátún H, Kristiansen R, Mortensen E, Østerhus S (2015) Transport of volume, heat, and salt towards the Arctic in the Faroe current 1993–2013. *Ocean Sci* 11(5):743–757. <https://doi.org/10.5194/os-11-743-2015>
- Hattermann T, Isachsen PE, Appen W, Albretsen J, Sundfjord A (2016) Eddy-driven recirculation of Atlantic Water in Fram Strait. *Geophys Res Lett* 43:1–9. <https://doi.org/10.1002/2016GL068323>
- Huang J, Pickart RS, Huang RX, Lin P, Brakstad A, Xu F (2020) Sources and upstream pathways of the densest overflow water in the Nordic Seas. *Nat Commun*. <https://doi.org/10.1038/s41467-020-19050-y>

- Hunke EC, Dukowicz JK (1997) An elastic–viscous–plastic model for sea ice dynamics. *J Phys Oceanogr* 27(9):1849–1867. [https://doi.org/10.1175/1520-0485\(1997\)027%3c1849:aevpmf%3e2.0.co;2](https://doi.org/10.1175/1520-0485(1997)027%3c1849:aevpmf%3e2.0.co;2)
- Ivanov VV, Alexeev VA, Repina I, Koldunov NV, Smirnov A (2012) Tracing Atlantic water signature in the Arctic sea ice cover east of Svalbard. *Adv Meteorol* 2012:1–11. <https://doi.org/10.1155/2012/201818>
- Ivanov V, Alexeev V, Koldunov NV, Repina I, Sandø AB, Smedsrud LH, Smirnov A (2016) Arctic ocean heat impact on regional ice decay: a suggested positive feedback. *J Phys Oceanogr* 46(5):1437–1456. <https://doi.org/10.1175/jpo-d-15-0144.1>
- Ivanov V, Smirnov A, Alexeev V, Koldunov NV, Repina I, Semenov V (2018) Contribution of convection-induced heat flux to winter ice decay in the western Nansen Basin. *J Geophys Res Oceans* 123(9):6581–6597. <https://doi.org/10.1029/2018jc013995>
- Johannessen OM, Johannessen JA, Svendsen E, Shuchman RA, Campbell WJ, Josberger E (1987) Ice-edge eddies in the Fram Strait marginal ice zone. *Science* 236(4800):427–429. <https://doi.org/10.1126/science.236.4800.427>
- Jónsson S, Valdimarsson H (2012) Water mass transport variability to the North Icelandic shelf, 1994–2010. *ICES J Mar Sci* 69(5):809–815. <https://doi.org/10.1093/icesjms/fss024>
- Karpouzoglou T, De Steur L, Smedsrud LH, Sumata H (2022) Observed changes in the Arctic freshwater outflow in Fram Strait. *J Geophys Res Oceans*. <https://doi.org/10.1029/2021jc018122>
- Koenig Z, Provost C, Sennéchaël N, Garric G, Gascard JC (2017a) The Yermak Pass branch: a major pathway for the Atlantic water north of Svalbard? *J Geophys Res Oceans* 122(12):9332–9349. <https://doi.org/10.1002/2017JC013271>
- Koenig Z, Provost C, Villacieros-Robineau N, Sennéchaël N, Meyer A, Lellouche J-M, Garric G (2017b) Atlantic waters inflow north of Svalbard: Insights from IAOOS observations and Mercator Ocean global operational system during N-ICE2015. *J Geophys Res Oceans* 122(2):1254–1273. <https://doi.org/10.1002/2016jc012424>
- Koenig Z, Meyer A, Provost C, Sennéchaël N, Sundfjord A, Beguery L, Athanase M, Gascard J-C (2018) Cooling and freshening of the west Spitsbergen current by shelf-origin cold core lenses. *J Geophys Res Oceans* 123(11):8299–8312. <https://doi.org/10.1029/2018jc014463>
- Lique C, Thomas MD (2018) Latitudinal shift of the Atlantic meridional overturning circulation source regions under a warming climate. *Nat Clim Chang* 8(11):1013–1020. <https://doi.org/10.1038/s41558-018-0316-5>
- Lique C, Johnson HL, Plancherel Y (2018) Emergence of deep convection in the Arctic Ocean under a warming climate. *Clim Dyn* 50(9–10):3833–3847. <https://doi.org/10.1007/s00382-017-3849-9>
- Lozier MS, Li F, Bacon S, Bahr F, Bower AS, Cunningham SA, De Jong MF, De Steur L, Deyoung B, Fischer J, Gary SF, Greenan BJW, Holliday NP, Houk A, Houpert L, Inall ME, Johns WE, Johnson HL, Johnson C, Karstensen J, Koman G, Le Bras IA, Lin X, Mackay N, Marshall DP, Mercier H, Oltmanns M, Pickart RS, Ramsey AL, Rayner D, Straneo F, Thierry V, Torres DJ, Williams RG, Wilson C, Yang J, Yashayaev I, Zhao J (2019) A sea change in our view of overturning in the subpolar North Atlantic. *Science* 363(6426):516–521. <https://doi.org/10.1126/science.aau6592>
- Lundesgaard Ø, Sundfjord A, Lind S, Nilsen F, Renner AHH (2022) Import of Atlantic water and sea ice controls the ocean environment in the northern Barents Sea. *Ocean Sci* 18(5):1389–1418. <https://doi.org/10.5194/os-18-1389-2022>
- Lundesgaard Ø, Sundfjord A, Renner AHH (2021) Drivers of interannual sea ice concentration variability in the Atlantic water inflow region north of Svalbard. *J Geophys Res Oceans*. <https://doi.org/10.1029/2020jc016522>
- Madec G, the NEMO team (2016) Nemo ocean engine (Note du Pôle de modélisation). Institut Pierre-Simon Laplace (IPSL)
- Manucharyan GE, Thompson AF (2017) Submesoscale sea ice–ocean interactions in marginal ice zones. *J Geophys Res Oceans* 122(12):9455–9475. <https://doi.org/10.1002/2017jc012895>
- Melsheimer C, Spreen G (2019) AMSR2 ASI sea ice concentration data, Arctic, version 5.4 (NetCDF) (July 2012–December 2019). PANGAEA. <https://doi.org/10.1594/PANGAEA.898399>
- Menze S, Ingvaldsen RB, Haugan P, Fer I, Sundfjord A, Beszczynska-Moeller A, Falk-Petersen S (2019) Atlantic water pathways along the north-western Svalbard shelf mapped using vessel-mounted current profilers. *J Geophys Res Oceans* 124(3):1699–1716. <https://doi.org/10.1029/2018jc014299>
- Myers PG, Castro de la Guardia L, Fu C, Gillard LC, Grivault N, Hu X, Lee CM, Moore GWK, Pennelly C, Ribergaard MH, Roman-ski J (2021) Extreme high greenland blocking index leads to the reversal of Davis and nares strait net transport towards the Arctic ocean. *Geophys Res Lett* 48(17):e2021GL094178. <https://doi.org/10.1029/2021GL094178>
- Nilsen F, Skogseth R, Vaardal-Lunde J, Inall M (2016) A simple shelf circulation model: intrusion of Atlantic water on the West Spitsbergen Shelf. *J Phys Oceanogr* 46(4):1209–1230. <https://doi.org/10.1175/JPO-D-15-0058.1>
- Onarheim IH, Smedsrud LH, Ingvaldsen RB, Nilsen F (2014) Loss of sea ice during winter north of Svalbard. *Tellus Dyn Meteorol Oceanogr* 66(1):23933. <https://doi.org/10.3402/tellusa.v66.23933>
- Pérez-Hernández MD, Pickart RS, Pavlov V, Våge K, Ingvaldsen R, Sundfjord A, Renner AHH, Torres DJ, Erofeeva SY (2017) The Atlantic Water boundary current north of Svalbard in late summer. *J Geophys Res Oceans* 122(3):2269–2290. <https://doi.org/10.1002/2016jc012486>
- Pérez-Hernández MD, Pickart RS, Torres DJ, Bahr F, Sundfjord A, Ingvaldsen R, Renner AHH, Beszczynska-Möller A, von Appen WJ, Pavlov V (2019) Structure, transport, and seasonality of the Atlantic water boundary current north of Svalbard: results from a Yearlong Mooring Array. *J Geophys Res Oceans* 124(3):1679–1698. <https://doi.org/10.1029/2018JC014759>
- Polyakov IV, Timokhov LA, Alexeev VA, Bacon S, Dmitrenko IA, Fortier L, Frolov IE, Gascard JC, Hansen E, Ivanov VV, Laxon S, Mauritzen C, Perovich D, Shimada K, Simmons HL, Sokolov VT, Steele M, Toole J (2010) Arctic ocean warming contributes to reduced polar ice cap. *J Phys Oceanogr* 40(12):2743–2756. <https://doi.org/10.1175/2010JPO4339.1>
- Polyakov IV, Pnyushkov AV, Timokhov LA (2012) Warming of the intermediate Atlantic water of the Arctic Ocean in the 2000s. *J Clim* 25(23):8362–8370. <https://doi.org/10.1175/jcli-d-12-00266.1>
- Polyakov IV, Pnyushkov AV, Alkire MB, Ashik IM, Baumann TM, Carmack EC, Goszczko I, Guthrie J, Ivanov VV, Kanzow T, Krishfield R, Kwok R, Sundfjord A, Morison J, Rember R, Yulin A (2017) Greater role for Atlantic inflows on sea-ice loss in the Eurasian Basin of the Arctic Ocean. *Science* 356(6335):285–291. <https://doi.org/10.1126/science.aai8204>
- Rantanen M, Karpechko AY, Lipponen A, Nordling K, Hyvärinen O, Ruosteenoja K, Vihma T, Laaksonen A (2022) The Arctic has warmed nearly four times faster than the globe since 1979. *Commun Earth Environ*. <https://doi.org/10.1038/s43247-022-00498-3>
- Rudels B, Korhonen M, Schauer U, Pisarev S, Rabe B, Wisotzki A (2015) Circulation and transformation of Atlantic water in the Eurasian Basin and the contribution of the Fram Strait inflow branch to the Arctic Ocean heat budget. *Prog Oceanogr* 132:128–152. <https://doi.org/10.1016/j.poccean.2014.04.003>
- Schauer J, Hansen E (2008) Variation of measured heat flow through the fram strait between 1997 and 2006. *Arctic-Subarctic ocean fluxes*. Springer, Netherlands, pp 65–85

- Smith DC, Bird AA (1991) The interaction of an ocean eddy with an ice edge ocean jet in a marginal ice zone. *J Geophys Res* 96(C3):4675. <https://doi.org/10.1029/90jc02262>
- Smith GC, Roy F, Mann P, Dupont F, Brasnett B, Lemieux J-F, Larocche S, Bélair S (2014) A new atmospheric dataset for forcing ice-ocean models: evaluation of reforecasts using the Canadian global deterministic prediction system. *Q J R Meteorol Soc* 140(680):881–894. <https://doi.org/10.1002/qj.2194>
- Spreen G, Steur L, Divine D, Geland S, Hansen E, Kwok R (2020) Arctic sea ice volume export through Fram Strait from 1992 to 2014. *J Geophys Res Oceans*. <https://doi.org/10.1029/2019jc016039>
- Sumata H, De Steur L, Gerland S, Divine DV, Pavlova O (2022) Unprecedented decline of Arctic sea ice outflow in 2018. *Nat Commun*. <https://doi.org/10.1038/s41467-022-29470-7>
- Thomas MD, Tréguier A-M, Blanke B, Deshayes J, Voltaire A (2015) A Lagrangian method to isolate the impacts of mixed layer subduction on the meridional overturning circulation in a numerical model. *J Clim* 28(19):7503–7517. <https://doi.org/10.1175/jcli-d-14-00631.1>
- Timmermans M, Marshall J (2020) Understanding Arctic ocean circulation: a review of ocean dynamics in a changing climate. *J Geophys Res Oceans*. <https://doi.org/10.1029/2018jc014378>
- Våge K, Pickart RS, Pavlov V, Lin P, Torres DJ, Ingvaldsen R, Sundfjord A, Proshutinsky A (2016) The Atlantic water boundary current in the Nansen Basin: transport and mechanisms of lateral exchange. *J Geophys Res Oceans* 121(9):6946–6960. <https://doi.org/10.1002/2016jc011715>
- Wang Q, Koldunov NV, Danilov S, Sidorenko D, Wekerle C, Scholz P, Bashmachnikov IL, Jung T (2020) Eddy kinetic energy in the Arctic Ocean from a global simulation with a 1-km Arctic. *Geophys Res Lett*. <https://doi.org/10.1029/2020gl088550>
- Wang Q, Shu Q, Wang S, Beszczynska-Moeller A, Danilov S, Steur L, Haine TWN, Karcher M, Lee CM, Myers PG, Polyakov IV, Provost C, Skagseth Ø, Spreen G, Woodgate R (2023) A review of Arctic-subarctic ocean linkages: past changes, mechanisms, and future projections. *Ocean Land Atmos Res* 2:1–39. <https://doi.org/10.34133/olar.0013>
- Wekerle C, Wang Q, von Appen WJ, Danilov S, Schourup-Kristensen V, Jung T (2017) Eddy-resolving simulation of the Atlantic water circulation in the Fram Strait with focus on the seasonal cycle. *J Geophys Res Oceans* 122(11):8385–8405. <https://doi.org/10.1002/2017JC012974>
- Zhao M, Timmermans M-L, Cole S, Krishfield R, Proshutinsky A, Toole J (2014) Characterizing the eddy field in the Arctic Ocean halocline. *J Geophys Res Oceans* 119(12):8800–8817. <https://doi.org/10.1002/2014jc010488>

Publisher's Note Springer Nature remains neutral with regard to jurisdictional claims in published maps and institutional affiliations.